

Defect charging and resonant states in half-Heusler $\text{Nb}_{1-x}\text{Ti}_x\text{FeSb}$

Yefan Tian,¹ Farit G. Vagizov,^{1,2} Nader Ghassemi,¹ Wuyang Ren,^{3,4}
Hangtian Zhu,³ Zhiming Wang,⁴ Zhifeng Ren,³ and Joseph H. Ross, Jr.^{1,*}

¹*Department of Physics and Astronomy, Texas A&M University, College Station, TX 77843, USA*

²*Kazan Federal University, 18 Kremlyovskaya Street, Kazan 420008, Russia*

³*Department of Physics, University of Houston, Houston, TX 77204, USA*

⁴*Institute of Fundamental and Frontier Sciences,*

University of Electronic Science and Technology of China, Chengdu 610054, China

(Dated: December 23, 2019)

We report NMR and Mössbauer studies along with DFT calculations of $\text{Nb}_{1-x}\text{Ti}_x\text{FeSb}$ ($0 \leq x \leq 0.3$), one of the most promising thermoelectric systems. These studies provide local information about defect changes and atomic configurations in these heavily *p*-type materials. The NMR spin-lattice relaxation rate is dominated by an orbital contribution rather than spin contribution, which provides a good measure of states within the valence band. The changes of effective mass and carrier concentration for different substitution fractions indicate the importance of deep resonant states. Both the measured Knight shift and chemical shift are significantly larger than expected, which we discuss in terms of an enhancement of Pauli susceptibility and Van Vleck susceptibility due to a Coulomb enhancement mechanism. The Mössbauer spectra of Ti-substituted samples are analyzed to show small departures from a binomial distribution of substituted atoms, while for unsubstituted *p*-type NbFeSb, the amplitude of a Mössbauer satellite peak increases vs temperature, showing a *T*-dependent charging behavior of defects and the corresponding impurity band located around 30 meV above the valence band.

I. INTRODUCTION

The half-Heusler family, as one of the most fascinating intermetallic systems, has gained considerable attention in recent years due to their extraordinary thermoelectric performance and unconventional topological properties. Half-Heusler materials have a general formula XYZ (X representing one of the $(\text{III-V})_B$ element, Y a transition metal of the VIII_B , and Z a tetrel or pnictogen element) [1–3] with crystal structure shown in Fig. 1, and can be formally derived from the cubic Heusler phases XY_2Z by removing one of the two equivalent Y atoms, leading to a structural vacancy. The ideal valence electron concentration (VEC) of half-Heusler compounds is 8 or 18 electrons per formula unit [4–8], with semiconducting or semimetallic behavior often observed with $\text{VEC} = 18$ [2–5, 9]. With a rich combination of chemical elements, this feature leads to interesting properties, from nonmagnetic semiconductors to ferromagnetic half metals, as well as other anomalous behavior, including strongly correlated electrons and topological insulator behavior [10–12].

Within the discovered half-Heusler systems, NbFeSb has recently been of particular interest due to its excellent thermoelectric performance within the realm of earth abundant thermoelectric materials [13]. With various elements doped or substituted, NbFeSb-based semiconductors exhibit a large power factor, above $100 \mu\text{W cm}^{-1} \text{K}^{-2}$ [13–15]. Defects can control the transport properties of half-Heusler compounds, thus enabling the electronic behaviors to be tuned. However, native defects

can also counteract the desired effects or otherwise degrade the electronic response. The defect issue has been explored experimentally for several compounds, such as ZrNiSn and TiCoSb [16–18]. With multiple elemental substitutions, a number of different types of half-Heusler alloys have been designed and shown to have high figures of merit ($ZT > 1.5$) [19–22]. Based on these high- ZT half-Heusler alloys, thermoelectric generators thus have the potential to reach a high power-conversion efficiency [21–23], enhancing the prospect of future thermoelectric applications.

To analyze the underlying electronic and magnetic properties of $\text{Nb}_{1-x}\text{Ti}_x\text{FeSb}$, we performed ^{93}Nb and ^{121}Sb NMR and ^{57}Fe Mössbauer measurements as local probes for all sites aiming at a better understanding of these materials. From NMR measurements, we demonstrate the metallicity at the measured temperature range and Korringa relation in these substituted materials. Mössbauer spectra are mapped to different nearest-neighbor configurations of Fe atoms.

II. EXPERIMENTAL AND COMPUTATIONAL METHODS

Raw elements (Nb pieces, 99.9%, and Sb broken rods, 99.9%, Atlantic Metals & Alloy; Fe granules, 99.98%, and Ti foams, 99.9%, Alfa Aesar) were weighed stoichiometrically, and arc melted multiple times to form uniform ingots. The ingots were then ball milled (SPEX 8000M Mixer/Mill) for 3 h under Ar protection to produce nanopowders. The powders were then consolidated into disks via hot pressing at 80 MPa for 2 min at 1373 K. This process has been shown to yield uniform sam-

* jhross@tamu.edu

TABLE I. Substitution fraction (x), sample designation (label), actual chemical composition (from EPMA analysis), measured room-temperature carrier concentration (p) from Hall measurements and theoretical carrier concentration (p_{theo}).

x	label	Actual composition	p (10^{20} cm^{-3})	p_{theo} (10^{20} cm^{-3})	p/p_{theo}
0	NbFeSb-1050	NbFeSb ^a	0.9 ^a	-	-
0.05	Ti(0.05)	Nb _{0.94} Ti _{0.05} Fe _{1.01} Sb _{0.99} ^b	8.1 ^b	9.5	0.85
0.1	Ti(0.1)	Nb _{0.89} Ti _{0.1} Fe _{1.00} Sb _{0.99} ^b	15.2 ^b	19	0.80
0.2	Ti(0.2)	Nb _{0.8} Ti _{0.2} Fe _{1.02} Sb _{0.99} ^b	25.7 ^b	38	0.68
0.3	Ti(0.3)	Nb _{0.69} Ti _{0.3} Fe _{1.02} Sb _{0.98} ^b	30.3 ^b	57	0.40

^a From Ref. [24].

^b From Ref. [13].

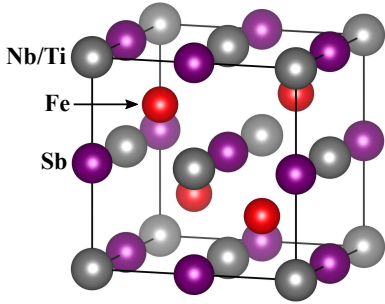


FIG. 1. Crystal structure of Ti-substituted half-Heusler $\text{Nb}_{1-x}\text{Ti}_x\text{FeSb}$, showing site occupations.

ples with high power factors [13]. In this work, we denote $\text{Nb}_{1-x}\text{Ti}_x\text{FeSb}$ as $\text{Ti}(x)$ ($x = 0.05, 0.1, 0.2, 0.3$). We also studied an unsubstituted sample, which is one of the samples described previously [24], annealed at 1323 K (sample NbFeSb-1050).

Substitution fractions, actual chemical compositions and carrier concentrations of all samples are listed in Table I. Room-temperature carrier concentrations were measured by Hall measurements [13] and shown to be p -type. Half-Heusler materials normally follow an 18-electron stability rule, and the balanced composition NbFeSb satisfies this criterion and is found to be a semiconductor. Cation substitution in the range ($\text{Nb}_{1-x}\text{Ti}_x$) leads to heavily p -type samples because Ti lacks one electron compared with Nb. In these samples, as expected, higher Ti fraction produces higher hole concentration, however the ratio of the measured charge density to the theoretical charge density becomes smaller with larger x as further discussed below.

Magnetic measurements were performed using a Quantum Design MPMS superconducting quantum interference device magnetometer. ^{93}Nb and ^{121}Sb NMR experiments were carried out by applying a custom-built pulse spectrometer at a fixed magnetic field 9 T using shift standards NbCl_5 and KSbF_6 in acetonitrile respectively, with positive shifts here denoting paramagnetic sign. Mössbauer spectra were measured at several temperatures in the range 80-323 K on a conventional con-

stant acceleration spectrometer (WissEl) equipped with a Co-57 source in rhodium matrix 35 mCi in activity. The spectrometer was calibrated using an α -iron foil at room temperature. Samples were prepared from fine $\text{Nb}_{1-x}\text{Ti}_x\text{FeSb}$ powders with the density of 18 mg of Fe per cm^2 uniformly distributed as a thin layer over sample holder. For low-temperature measurements, the samples were mounted on a cold finger of a helium continuous-flow cryostat CFICEV-MOSS, ICE Oxford, UK. The temperature of the sample was controlled within ± 0.5 K over the whole temperature range. The observed spectra were least-squares fitted with the assumption that line shapes are Lorentzian to yield the hyperfine parameters: isomer shift (IS) and quadrupole splitting (QS). Isomer shifts were referred to α -Fe at room temperature.

Density functional theory (DFT) calculations were performed with WIEN2k [25] using Perdew, Burke, and Ernzerhof (PBE) exchange-correlation potential, and a k -point grid of $10 \times 10 \times 10$, and lattice constants from the experimental values [24]. In calculations done without including spin-orbit coupling, a semiconducting gap of 0.54 eV was obtained. This can be compared to 0.51 eV obtained from transport measurements at high temperatures [13]. For the VB maximum at the L point, we also obtained an effective mass $m_{\text{eff}} = 4.9 m_e$ by fitting the density of states over a range up to 0.1 eV below the band edge. For ^{93}Nb NMR chemical shifts the zero offset was calibrated by a separate shift calculation for LaNbO_4 and for YNbO_4 , and then adjusted based on the previously reported shifts [26] to the standard reference (NbCl_5 in acetonitrile). Since chemical shifts are less well studied for ^{121}Sb , we did not find a comparable solid compound with which to calibrate the computational ^{121}Sb zero offset. We also performed a similar set of calculations with spin-orbit coupling included but found that the results are relatively insensitive to spin-orbit coupling – we found for example that with spin-orbit coupling the relative effective mass increases from 4.9 to 5.0, while the calculated ^{93}Nb chemical shifts changed by less than 60 ppm.

III. EXPERIMENTAL RESULTS

A. NMR measurements

1. Line shapes

Fig. 2 shows the ^{93}Nb and ^{121}Sb NMR line shapes of the $\text{Ti}(x)$ samples obtained from the fast Fourier transform of the spin echo using a standard $\pi/2-\tau-\pi$ sequence. Also superposed are the resonances for the $x = 0$ sample NbFeSb-1050 with a much smaller room-temperature carrier concentration ($p = 9 \times 10^{19} \text{ cm}^{-3}$) [24]. It can be seen from the superposed spectra that there is a small signal due to pure-phase NbFeSb , which appears only for the $\text{Ti}(0.05)$ substituted sample. The resonances for both nuclei become broader and move to lower frequencies when the substitution fraction increases. These effects are due to a combination of Knight shifts and chemical shifts, as discussed below.

The increasing line width vs x is due to a superposition of local environments at Nb and Sb sites. For Nb, the first and second neighbor shells are composed of Fe and Sb ions respectively, so it is only starting with the third shell that the (Nb, Ti) substitution produces a distribution of local environments. Correspondingly, for Sb the first neighbor shell consisting of Fe ions is fixed, while the second neighbors will include a distribution of (Nb, Ti) ions. This leads to relatively symmetric local environments, with a large number of (Nb, Ti) configurations contributing to the observed line widths. Since the widths scale nearly proportionally to the differences in NMR shift relative to NbFeSb , with the Sb widths and shifts considerably smaller, we surmise that the widths are due to a quasi-random superposition of chemical and Knight shifts. As quadrupolar nuclei, it is also possible for a second-order quadrupole contribution to contribute to the mean shift, however with this mechanism contributing a small fraction of the observed widths this contribution will be small. For example, Nb oxides having a nearly symmetric first-neighbor shell are found to have ^{93}Nb quadrupole parameters ν_Q less than 1 MHz [26], which would yield [27] a mean shift contribution of about 50 ppm. This is 2% of the mean shift for the $\text{Ti}(0.3)$ sample, and is presumably an upper limit, so we neglect such contributions in analyzing the relative shifts. The result is a sum of anisotropic Knight shift (K) and chemical shift (δ) with δ due to the orbital susceptibility and K associated with the spin susceptibility of the carriers.

2. Shifts

The ^{93}Nb and ^{121}Sb first moments for all samples, measured at room temperature, are shown in Fig. 3(a). These are the center-of-mass isotropic positions of the measured spectra. For samples sufficiently doped to exhibit metal-

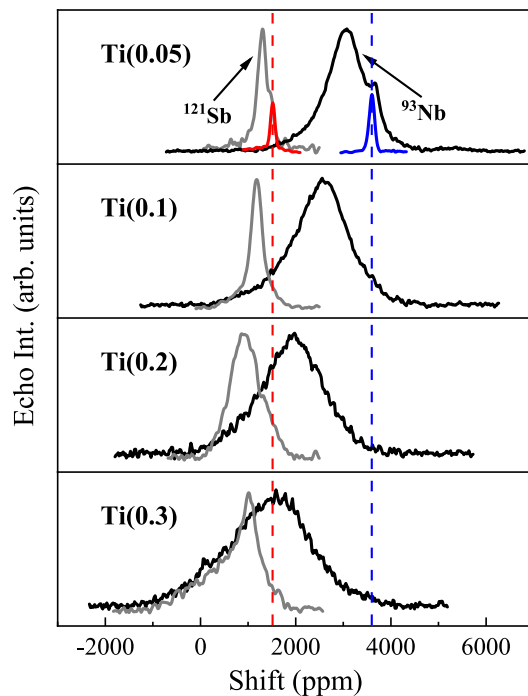


FIG. 2. Room-temperature ^{93}Nb (black) and ^{121}Sb (gray) NMR line shapes for $\text{Ti}(x)$ ($x = 0.05, 0.1, 0.2, 0.3$) samples. The ^{93}Nb spectrum of NbFeSb previously reported [24] is shown in blue solid curve for comparison with Ti -substituted NbFeSb , and a ^{121}Sb spectrum is also shown measured for the same sample in red. Dashed lines show the shift positions of sample NbFeSb-1050 [24].

lic behavior, K can be given generally as,

$$K \equiv \frac{\Delta\nu}{\nu_0} = \frac{H_{\text{HF}}\chi_P}{\mu_B}, \quad (1)$$

where H_{HF} is the relevant hyperfine coupling field constant and χ_P is the Pauli electron spin susceptibility per atom, $g(E_F)(g_{\text{eff}}/2)\mu_B^2$. g_{eff} is the effective g -factor due to spin-orbit coupling, which can modify the energy splitting and also K . For s -character conduction electron states, the dominant hyperfine interaction will be Fermi contact. However, with d electrons dominant here, the core polarization hyperfine field H_{CP} is the relevant spin coupling with the dipolar spin contribution to K vanishing in cubic symmetry. Note also that we assume spin-orbit coupling effects are small in these materials. As a result, K can be expressed as

$$K = g_{\text{partial}}(E_F)\left(\frac{g_{\text{eff}}}{2}\right)\mu_B H_{\text{CP}}, \quad (2)$$

where $g_{\text{partial}}(E_F)$ is the Fermi-level partial density of states for the atom containing the nucleus being measured.

In an effective mass approximation, which is often appropriate for semiconductors, it is found in the metallic limit,

$$g(E_F) = m_{\text{eff}} \frac{(3\pi^2 n)^{1/3}}{\pi^2 \hbar^2} V_{\text{f.u.}}, \quad (3)$$

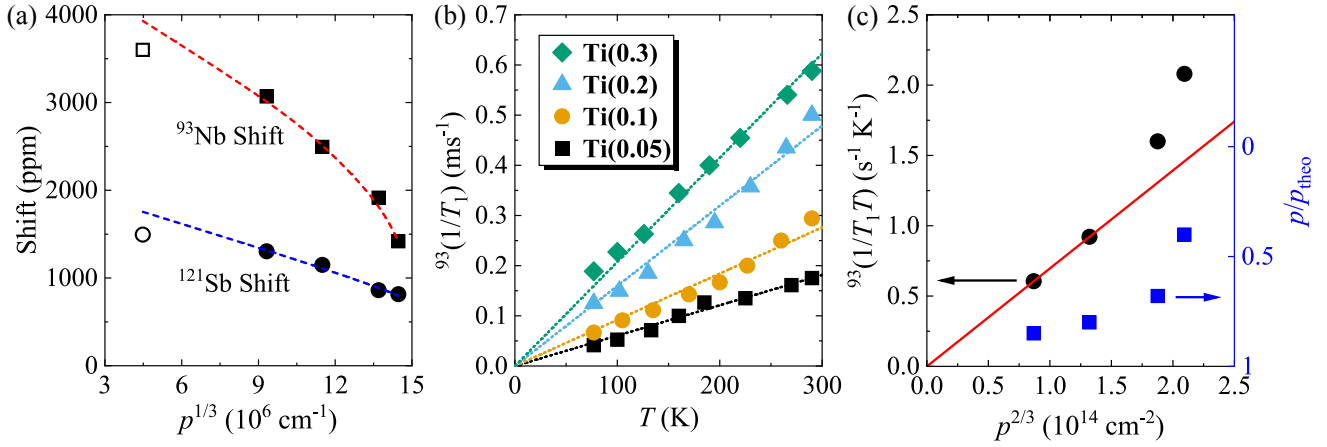


FIG. 3. (a) Total shifts of ^{93}Nb and ^{121}Sb vs $p^{1/3}$ at room temperature, where p is the measured hole density. Dashed lines are the fits to the experimental data described in the text. Open symbols: NbFeSb-1050 sample. (b) Temperature dependence of relaxation rates for ^{93}Nb in Ti(x) samples, indicated by squares, triangles, circles, and diamonds for $x = 0.05, 0.1, 0.2, 0.3$ respectively, with fits to metallic behavior as described in the text. (c) $^{93}(1/T_1T)$ vs $p^{2/3}$ at room temperature with fit to constant effective mass behavior. Also shown: p/p_{theo} vs $p^{2/3}$.

where m_{eff} is the thermodynamic effective mass, n is the carrier density and $V_{\text{f.u.}}$ is the volume per formula unit. Thus substituting Eq. (3) into Eq. (2), K should scale as $p^{1/3}$. As shown in Ref. [28], the chemical shift of $\text{Cd}_{1-x}\text{Zn}_x\text{Te}$ is linearly dependent on x , indicating a linear relationship between substitution fraction and chemical shift similar to other properties often observed in semiconductor alloys. $\delta(x)$ is thus assumed to be linearly dependent on the substitution fraction of Ti. We therefore model the shift as,

$$\begin{aligned} (\text{Total Shift}) &= K(p) + \delta(x) \\ &= A \cdot p^{1/3} + B \cdot x + C \end{aligned} \quad (4)$$

where $A = \frac{(3\pi^2)^{1/3}}{\pi^2 \hbar^2} \left(\frac{g_{\text{eff}}}{2} \right) m_{\text{eff}} \mu_B H_{\text{CP}}$ and C represents the baseline shift, corresponding to the Fermi level at the mid-gap for pure NbFeSb. Fitted curves are shown in Fig. 3(a) corresponding to the total ^{93}Nb and ^{121}Sb shifts fit to Eq. (4). This yields the fitting parameters for Nb $A = -1.5 \times 10^{-4} \text{ cm}$, $B = -3352$ and $C = 4607$; and for Sb $A = -8.8 \times 10^{-5} \text{ cm}$, $B = -256$ and $C = 2149$, all in ppm shift units.

The fitted results indicate a large ^{93}Nb chemical shift of $\delta = 4607 \text{ ppm}$ for NbFeSb, decreasing rapidly vs x . The $x = 0$ result is 600 ppm larger than previously obtained [24] since here we are able to better separate the Knight shift part of the shift. The ^{93}Nb shifts are quite large; the calculated ^{93}Nb chemical shift, with the offset for the reference standard calibrated against LaNbO_4 and YNbO_4 , is $\delta = 3220 \text{ ppm}$, a considerably smaller value. A similar calculation for the semi-Heusler compound NbCoSn yielded a ^{93}Nb chemical shift of 2585 ppm, in much closer agreement with the measured value, $\delta = 2849 \text{ ppm}$ [29]. The fitted results also indicate a 256 ppm reduction in ^{121}Sb chemical shift going from NbFeSb to TiFeSb. In comparison, the ^{121}Sb chemical

shifts calculated using the WIEN2k package decrease by 132 ppm, following the same trend vs substitution as the measured results. However, the ^{93}Nb result exceeds the usual range of reported shifts, and here we see that it is significantly larger than obtained by DFT.

3. Spin-lattice relaxation rates

The ^{93}Nb spin-lattice relaxation rate, denoted as $^{93}(1/T_1)$, was measured using the inversion recovery method in the T range of 77-290 K. The recovery of the ^{93}Nb central-transition magnetization can be expressed as

$$\begin{aligned} \frac{M(t) - M(\infty)}{M(\infty)} &= -2\alpha(0.152e^{-\frac{t}{T_1}} + 0.14e^{-\frac{6t}{T_1}} \\ &\quad + 0.153e^{-\frac{15t}{T_1}} + 0.192e^{-\frac{28t}{T_1}} + 0.363e^{-\frac{45t}{T_1}}). \end{aligned} \quad (5)$$

Here, $M(t)$ is the measured signal at the recovery time t . Each experimental T_1 value was obtained by a fit to this multi-exponential recovery curve. For all studied compounds, the $^{93}(1/T_1)$ results exhibit a constant T_1T behavior, indicating a metallic-type relaxation process as shown in Fig. 3(b) confirming that these compositions behave like metals. In the case that an effective mass treatment is appropriate, from an analysis similar to what is given above for K one finds that $1/T_{1K}$ should scale as $p^{2/3}$. As shown in Fig. 3(c), $^{93}(1/T_{1K})$ of the Ti(x) samples follows a linear dependence on $p^{2/3}$ for smaller p , although there is an enhancement for large p , which is further discussed below.

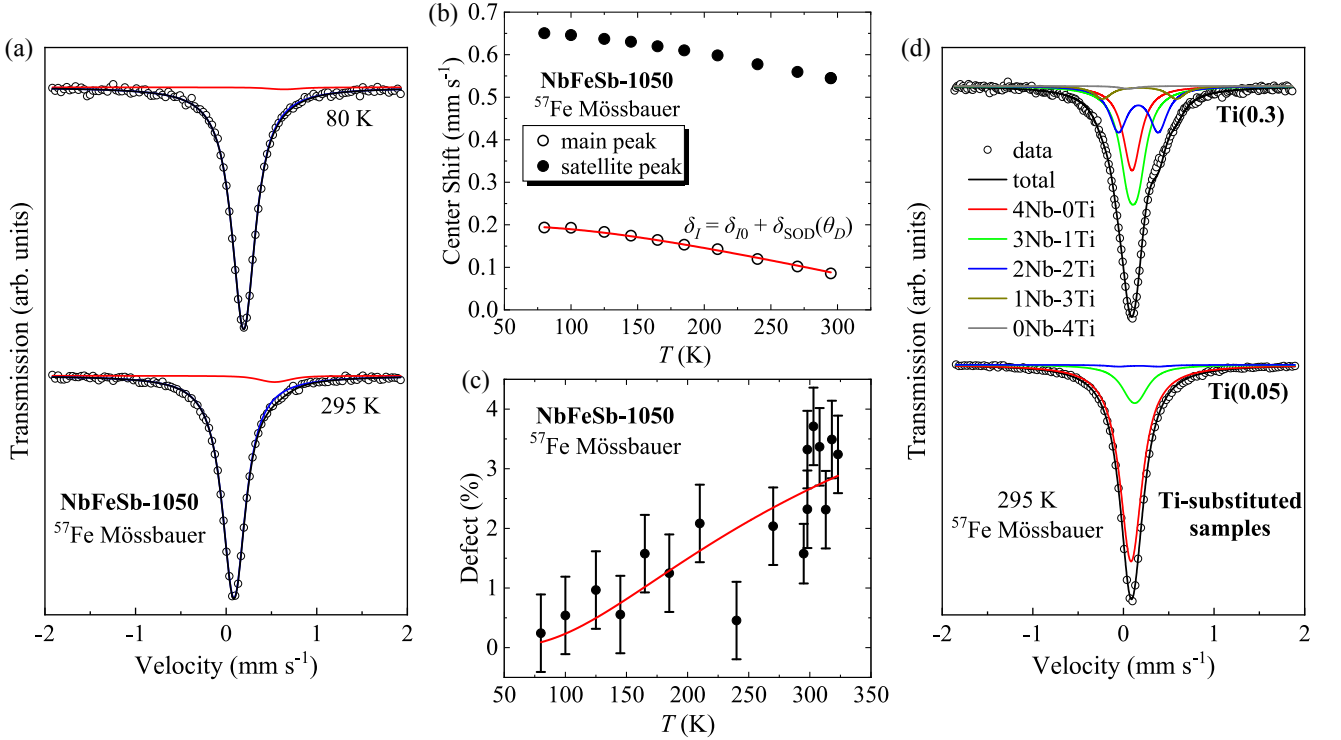


FIG. 4. (a) ^{57}Fe Mössbauer spectra for unsubstituted NbFeSb-1050 sample with least-squares fits described in the text plotted as solid curves. Velocities are relative to metallic iron ($\alpha\text{-Fe}$). Error bars are too small to be seen. The overall fitted curve and the two fitted peaks are plotted separately. (b) Shift vs temperature for the main peak and satellite peak in NbFeSb-1050 Mössbauer spectrum with Debye model fit. (c) Charged defect concentration of NbFeSb-1050 vs temperature from fit of satellite peak. (d) ^{57}Fe Mössbauer spectrum of Ti(0.3) and Ti(0.05) samples. Solid curves are fits for local environments of Fe atoms as shown. 3Nb-1Ti and 4Nb-0Ti configurations are negligible for Ti(0.05) due to their small contribution to the spectrum.

B. Mössbauer measurements

Fig. 4(a) shows Mössbauer spectra for the unsubstituted NbFeSb-1050 sample at 80 and 295 K. Both spectra show no sign of magnetic splitting. Least-square fitting curves are also shown in the figure. In both cases, a good fit was obtained using two Voigt lines, including a main peak and a small satellite with about 0.5 mm s^{-1} larger shift. The line widths thus determined are nearly temperature independent, with FWHM 0.302 mm s^{-1} for the main line at 295 K, increasing to 0.318 mm s^{-1} at 80 K. These small line widths indicate a lack of inhomogeneous broadening, showing NbFeSb to be well-ordered in the half-Heusler structure. The T -dependent shifts for the two fitted peaks are shown in Fig. 4(b), gradually decreasing with temperature increasing. The main line shift is 0.089 mm s^{-1} at 295 K and 0.194 mm s^{-1} at 80 K. These results are very similar to the results recently reported [30] for an n -type NbFeSb sample. A fit to a standard second-order doppler relation [31], shown in Fig. 4(b), yields $\theta_D = 488(6) \text{ K}$, and a $T = 0$ isomer shift $\delta_I = 0.199 \text{ mm s}^{-1}$. While it is possible for δ_I to have a small temperature dependence, comparison to $\theta_D \cong 380 \text{ K}$ obtained from specific heat measurements [24, 32] apparently reflect a larger vibrational displacement

for the Fe ion, producing the change in Mossbauer shift, vs specific heat which measures essentially an average vibrational displacement.

The amplitude of the fitted small satellite changes vs T , indicating a change in the charge state of a native defect vs temperature. Fig. 4(c) shows the spectral area of the satellite peak, as a percentage of the main peak area, corresponding to the relative concentration of Fe ions participating in these defects. When temperature increases, the defect concentration shows an upturn corresponding to the excitation of carriers out of the defect level. The result was fit to the acceptor density function [33],

$$N_a^+ = \frac{N_A}{1 + 4 \cdot e^{\Delta/kT}}, \quad (6)$$

assuming each neutral acceptor contains two electrons with opposite spins and the state with no electron is prohibited, and where Δ is the energy difference between defect level and chemical potential. The fitting [Fig. 4(c)] gives $\Delta = 30 \text{ meV}$. This is in good agreement with the result previously obtained from NMR [24], in which the spin-lattice relaxation rate of NbFeSb also shows a sharp increase close to room temperature. This confirms the existence of a large density of shallow defects located about 30 meV above the valence band in the p -type samples.

Figs. 4(d) shows the ^{57}Fe Mössbauer spectra of Ti(0.3) and Ti(0.05) respectively at room temperature. For Fe atoms (4c sites) in $\text{Nb}_{1-x}\text{Ti}_x\text{FeSb}$ alloys, 4 out of 8 nearest-neighbor sites are occupied by mixed Nb and Ti atoms. Thus, the resulting spectra can be modeled as superpositions of individual spectra for different local configurations of these neighbor ions. The spectrum was then fit to individual peaks with amplitudes corresponding to a binomial distribution,

$$P_n(x) = \frac{4!}{n!(4-n)!} x^n (1-x)^{4-n}, \quad (7)$$

for the probability of each Nb-Ti configuration. For the Ti(0.3) sample, probabilities are 24, 41, 26, 7.6, and 0.8%, for 0 through 4 Ti ions respectively, occupying the 4 Nb/Ti neighbor sites. However, after first fixing these areas in the fit, we found that a better fit with good-ness of fit (χ^2) decreasing from 1.58 to 0.98 has a slightly modified distribution, with the probabilities changed to 26.5, 44.8, 19.8, 8.0, and 0.9%, for the same neighbor configurations, indicating a reduced probability for the 2Nb-2Ti configuration in favor of the others. This could be an indication of the segregation of Nb and Ti neighbors for larger substitution amounts. On the other hand, for the Ti(0.05) sample, the standard binomial probabilities, 81.4, 17.1, and 1.3% for 0 through 2 Ti-ion neighbors respectively, with negligible contributions for 3 and 4 neighbors, worked very well in fitting the data. In these fits, the 4Nb-0Ti neighbor peaks have very similar center shifts of 0.087 and 0.085 mm s^{-1} , for Ti(0.3) and Ti(0.05) respectively, and these are very close to the room-temperature shifts observed in the unsubstituted sample. The increasing isomer shift for larger number of Ti neighbors, for example 0.17 mm s^{-1} for 2Nb-2Ti in Ti(0.3), is an indication of enhanced d -electron transfer to Fe in these configurations.

C. Magnetic measurements

The magnetic susceptibility (χ) of the sample with the largest Ti concentration, Ti(0.3), is shown in Fig. 5(a), for a fixed field of 1000 Oe. We fit the low- T data to a Curie-Weiss function according to the standard relationship, $\chi(T) = C/(T-T_C) + \chi_0$, where $C = N_A c p_{\text{eff}}^2 \mu_B^2 / 3k_B$ is the Curie constant with c the concentration of magnetic ions and p_{eff} the effective moment. The results are $T_C = -1.4$ K and assuming $p_{\text{eff}} = 3/2$ (see below), a dilute concentration $c = 0.96\%$ of these moments.

M vs H measurements confirm that the magnetic response is due to dilute paramagnetic defects, as shown at $T = 5$ K in Fig. 5(b) for sample Ti(0.3). To analyze for the local magnetic moments, data were fit to

$$M = N_A c g J \mu_B B_J(x), \quad (8)$$

where $B_J(x)$ is a Brillouin function with $x = \frac{g \mu_B J B}{k_B T}$. Assuming $g = 2$ expected for transition ions, we found that

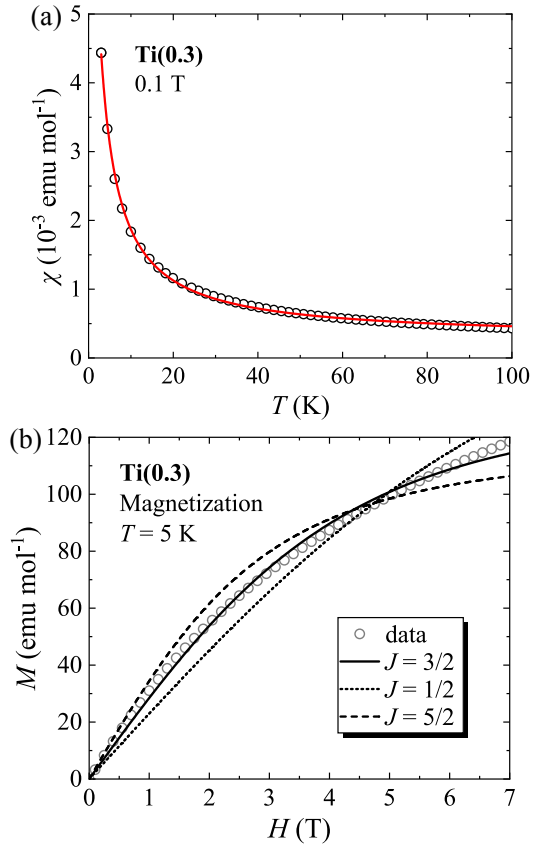


FIG. 5. Magnetic measurements for sample Ti(0.3). (a) Susceptibility vs T from 3 to 100 K with fit described in text. (b) M vs H measured at 5 K. Brillouin function fit is shown with $J = 1/2$ and $J = 5/2$ curves for comparison.

$J = 3/2$ gives the best agreement [Fig. 5(b)]. Thus fixing $J = 3/2$, the fit gives $c = 0.008$ per formula unit, which agrees well with the value obtained from M - T measurement.

The very small density of moments obtained here is comparable to what was obtained in annealed unsubstituted NbFeSb samples [24], for example 0.002 per formula unit in sample NbFeSb-1050. Thus we see that there is almost no tendency for Ti substitution to promote magnetic defect formation. Note also that $\text{TeFe}_{1+x}\text{Sb}$ semi-Heusler alloys [34, 35] close to the stable $\text{TeFe}_{1.33}\text{Sb}$ composition, with Fe interstitials which balance the missing charge of the Ti ions to achieve 18-electron balance, a large Curie-type response is observed. However, the latter apparently corresponds to only a few percent of the Fe sites, with the bulk of the material non-magnetic, as confirmed by Mössbauer results [35]. It is interesting that in the compositions studied here, even with substitution of 30% Ti for Nb breaking the 18-electron stability rule, there are not significant numbers of Fe interstitials, based on the EPMA results. However, by analogy with the $\text{TeFe}_{1.33}\text{Sb}$ results quoted above such defects are likely to be nonmagnetic, and perhaps these are the source of the band of defects indicated by the

Mossbauer results. As before [24] a likely candidate for the dilute-magnetic $J = 3/2$ defects would be Fe anti-sites on Nb positions. Note also that a small paramagnetic peak [24] might also be expected in the NMR $1/T_1$ [Fig. 3(b)], however here the relaxation rate is strongly dominated by a larger $1/T_1$ contribution due to the carriers in the substituted samples.

IV. DISCUSSION

The observed variation in amplitude of the satellite ^{57}Fe Mössbauer peak in NbFeSb is an unusual feature corresponding to a relatively large density of defects. As shown above, this is consistent with the existence of an impurity band shown also in the NMR results [24]. The temperature dependence of ^{57}Fe Mössbauer absorption area shows that the origin of the impurity band is Fe-related, probably due to Fe interstitials [24].

Besides our work, Hobbis *et al.* [30] also reported ^{57}Fe Mössbauer spectroscopy of NbFeSb, however in contrast with the p -type NbFeSb-1050 sample, their work focused on n -type NbFeSb. For n -type NbFeSb, two extra small doublets were observed with positions that differ from that of our measured satellite (0.65 mm s^{-1}). These different behaviors indicate different types of defects, which is reasonable given the different carrier types.

Comparing to other ^{57}Fe Mössbauer results for different materials within the half-Heusler family, for VFeSb, only a single line was observed with an isomer shift of $\sim 0.05 \text{ mm s}^{-1}$ with no extra peaks [36]. In Ref. [35], ^{57}Fe Mössbauer of $\text{TiFe}_{1.33}\text{Sb}$ also shows two sets of peaks, a doublet (main peak) with an isomer shift 0.108 mm s^{-1} and a singlet with an isomer shift 0.211 mm s^{-1} (satellite peak). These were matched to certain local atomic arrangement close to Fe atoms, indicating nonrandomness of Fe atoms on the $4d$ site. The larger shifts then observed for NbFeSb are consistent with the results found here for $\text{Nb}_{1-x}\text{Ti}_x\text{FeSb}$, with an isomer shift which is enhanced as the number of Ti neighbors increases.

In transition metals, besides the contribution from the spin moments of the conduction electrons, the orbital contribution to the NMR relaxation caused by fluctuating orbital moments of the conduction electrons can also make an important contribution to $1/T_1$. In this case, the spin-lattice relaxation rate should be dominated by two terms: $(1/T_1)_{\text{total}} = (1/T_1)_{\text{orb}} + (1/T_1)_d$, where the first term is orbital contribution term $(1/T_1)_{\text{orb}}$ and the second is d -spin relaxation rate $(1/T_1)_d$.

For transition metals with cubic structure, the orbital relaxation rate can be expressed in a general form [37],

$$(1/T_1)_{\text{orb}} = 2A \frac{2\pi}{\hbar} [\gamma_e \gamma_n \hbar^2 g_{\text{Nb}}(E_F) \langle r^{-3} \rangle]^2 k_B T, \quad (9)$$

where $A = 10C(2 - C)$ is a dimensionless quantity with C the degree of admixture of Γ_5 and Γ_3 symmetry at the Fermi level and $\langle r^{-3} \rangle$ is the average over occupied d

orbitals which would be expected [38] for NbFeSb to include only local contributions. It was shown in Ref. [37] that the orbital relaxation term for d -band metals reaches a maximum with a specific admixture of d orbitals corresponding to $\Gamma_5 : \Gamma_3 = 3 : 2$. Our DFT calculation shows that the ratio of atomic functions for NbFeSb is $t_{2g}(\Gamma_5) : e_g(\Gamma_3) = 68\% : 32\%$, giving $A = 9.8$ close to the maximum value 10, while for Nb, the calculated $g(E)$ near the VB edge is 14% of the total. Since, as shown below, the orbital $(1/T_1)_{\text{orb}}$ is found to dominate, we examine the dependence on Ti substitution. In Fig. 3(c), the solid line uses Eq. (9) as a fitting function with $g(E_F)$ expressed by Eq. (3). Using $\langle r^{-3} \rangle = 1.84 \times 10^{25} \text{ cm}^{-3}$ [39], the fit [Fig. 3(c)] to low-substituted samples gives $m_{\text{eff}} = 4.6 m_e$ in a good agreement with the calculated $m_{\text{eff}} = 4.9 m_e$ for NbFeSb.

The core polarization contribution to the d -spin spin-lattice relaxation rate in metals is

$$(1/T_1)_d = 2\hbar k_B T [\gamma_n H_{\text{CP}} g_{\text{Nb}}(E_F)]^2 q, \quad (10)$$

where the core polarization hyperfine field H_{CP} is reported to be -21 T [40] and q is a reduction factor which is a function of the admixture of d orbitals. In the present case, for nearly uniform occupation of the five d orbitals, $q \approx 1/5$ [40]. Using $g_{\text{Nb}}(E_F) = 0.243 \text{ states/eV}$ calculated as described above, Eq. (10) gives the spin contribution $(1/T_1 T)_d = 0.016 \text{ s}^{-1} \text{ K}^{-1}$ with the value for the low-substituted samples, $m_{\text{eff}} = 4.6 m_e$, inserted in Eq. (3). There is also a dipole spin contribution to $1/T_1$, however for the large d -orbital degeneracy case, this can be shown [40] to be much smaller than the orbital contribution. These results show that the orbital contribution is the dominant term in the spin-lattice relaxation process.

For low-substituted samples, the solid line shown in Fig. 3(c) is a fit to Eq. (9) yielding $m_{\text{eff}} = 4.6 m_e$ as stated above. When the Ti fraction goes up to 30%, the upturn of $1/T_1 T$ could correspond to an effective mass increase to $5.5 m_e$. At the same time, there is a decrease in the measured hole density relative to p_{theo} , as also shown in Fig. 3(c). Non-parabolicity of the valence band could explain the small increase in m_{eff} , however such an effect would not be expected to affect the Hall-effect results, at least in the spherical hole pocket limit. Thus, we conclude that the presence of resonant states in the valence band [41] becomes important for large x , an effect which would explain both observed results. In this case, for large x , the Fermi level moves more deeply into the valence band encountering resonant states caused by Ti substitutions. This effect could have significance for thermoelectric properties, however for smaller x , the agreement between theory and experiment indicates that such effects are not important near the band edge, and thus a rigid-band effective mass model provides a good description for the less-heavily substituted compositions.

For $\text{Ti}(x)$ samples, the measured Knight shift values are also found to be larger than expected. For example, the Knight shift contribution to the total shift for

the Ti(0.3) sample is -2185 ppm from our fit. However, using $g_{\text{Nb}}(E_F) = 0.243$ states/eV obtained above and the core polarization hyperfine field $H_{\text{CP}} = -21$ T, Eq. (2) gives $K = -295$ ppm. The Knight shift difference could be explained by a large g_{eff} in these samples, or by electron-electron interactions which can also enhance the measured spin susceptibility and thereby the Knight shift.

In addition to the observed large Knight shifts, the ^{93}Nb chemical shifts (δ) also show relatively large values as note above. The DFT calculations give the ^{93}Nb chemical shift as 3268 ppm. However, as noted above the fitted chemical shift for NbFeSb is 4607 ppm. The difference corresponds to an enhancement of the local orbital hyperfine field which is due to a Van Vleck susceptibility (χ_{VV}). In addition to the well-known enhancement of the spin susceptibility, electron-electron interactions can also lead to an enhancement of χ_{VV} [42, 43], thus yielding a large chemical shift. Ref. [43] also pointed out that orbital degeneracy is necessary for this effect which is already take into consideration in $1/T_1T$ of these samples. Thus, although the calculated distribution of d electrons in the valence band for Nb and Fe provide good agreement with the observed orbital T_1 , as a measure of the local susceptibilities the NMR shifts demonstrate that electron-electron interaction effects are relatively strong for these states.

V. CONCLUSIONS

In this work, we have investigated the effect of defects and substitutions of NbFeSb using local NMR and Mössbauer probes. The spin-lattice relaxation rate is found to be dominated by an orbital contribution with the spin contribution being negligible, which provides further information about the band-edge states for substituted samples. The effective mass and carrier concentration vs substitution reveal information about resonant levels. NMR shifts of Ti-substituted NbFeSb samples are well-explained by a model combining carrier-concentration-dependent Knight shift and composition-dependent chemical shift. Both the Pauli and Van Vleck susceptibilities are significantly enhanced, and these results indicate the importance of electron-electron interaction contribution. The T -dependence of the satellite peak in the unsubstituted NbFeSb Mössbauer spectrum provides a direct measure of acceptor charging with the corresponding impurity band located around 30 meV above valence band edge, while the Mössbauer spectrum of Ti(0.3) departures from binomial distribution, indicate a small deviation from random substitution in the mixed alloys, which reveals a possible segregation of 4a-site substitution atoms in half-Heusler materials.

ACKNOWLEDGMENTS

This work is supported by the Robert A. Welch Foundation, Grant No. A-1526. F. G. V. also acknowledges the support by National Science Foundation, Grant No. PHY-150-64-67.

-
- [1] M. A. Kouacou, J. Pierre, and R. V. Skolozdra, *J. Phys. Condens. Matter* **7**, 7373 (1995).
 - [2] J. Pierre, R. V. Skolozdra, J. Tobola, S. Kaprzyk, C. Hordequin, M. A. Kouacou, I. Karla, R. Currat, and E. Lelievre-Berna, *J. Alloys Compd.* **262**, 101 (1997).
 - [3] J. Tobola, J. Pierre, S. Kaprzyk, R. V. Skolozdra, and M. A. Kouacou, *J. Phys. Condens. Matter* **10**, 1013 (1998).
 - [4] F. G. Aliev, N. B. Brandt, V. V. Moshchalkov, V. V. Kozyrkov, R. V. Skolozdra, and A. I. Belogorokhov, *Z. Phys.* **75**, 167 (1989).
 - [5] F. G. Aliev, V. V. Kozyrkov, V. V. Moshchalkov, R. V. Skolozdra, and K. Durczewski, *Z. Phys.* **80**, 353 (1990).
 - [6] D. P. Young, P. Khalifah, R. J. Cava, and A. P. Ramirez, *J. Appl. Phys.* **87**, 317 (2000).
 - [7] H. C. Kandpal, C. Felser, and R. Seshadri, *J. Phys. D* **39**, 776 (2006).
 - [8] T. Graf, C. Felser, and S. S. P. Parkin, *Prog. Solid State Chem.* **39**, 1 (2011).
 - [9] H. Hohl, A. P. Ramirez, C. Goldmann, G. Ernst, B. Wölfling, and E. Bucher, *J. Phys. Condens. Matter* **11**, 1697 (1999).
 - [10] C. Shi, X. Xi, Z. Hou, X. Zhang, G. Xu, E. Liu, W. Wang, W. Wang, J. Chen, and G. Wu, *Phys. Status Solidi* **252**, 357 (2015).
 - [11] B. Nowak and D. Kaczorowski, *J. Phys. Chem. C* **118**, 18021 (2014).
 - [12] X. Zhang, Z. Hou, Y. Wang, G. Xu, C. Shi, E. Liu, X. Xi, W. Wang, G. Wu, and X.-x. Zhang, *Sci. Rep.* **6**, 23172 (2016).
 - [13] R. He, D. Kraemer, J. Mao, L. Zeng, Q. Jie, Y. Lan, C. Li, J. Shuai, H. S. Kim, Y. Liu, et al., *Proc. Natl. Acad. Sci. U.S.A.* **113**, 13576 (2016).
 - [14] W. Ren, H. Zhu, Q. Zhu, U. Saparamadu, R. He, Z. Liu, J. Mao, C. Wang, K. Nielsch, Z. Wang, et al., *Adv. Sci.* **5**, 1800278 (2018).
 - [15] J. Yu, C. Fu, Y. Liu, K. Xia, U. Aydemir, T. C. Chasapis, G. J. Snyder, X. Zhao, and T. Zhu, *Adv. Energy Mater.* **8**, 1701313 (2018).
 - [16] C. Uher, J. Yang, S. Hu, D. T. Morelli, and G. P. Meisner, *Phys. Rev. B* **59**, 8615 (1999).
 - [17] M. Wambach, R. Stern, S. Bhattacharya, P. Ziolkowski, E. Müller, G. K. Madsen, and A. Ludwig, *Adv. Electron. Mater.* **2**, 21500208 (2016).
 - [18] G. J. Snyder and E. S. Toberer, *Nat. Mater.* **7**, 105 (2008).
 - [19] C. Fu, S. Bai, Y. Liu, Y. Tang, L. Chen, X. Zhao, and T. Zhu, *Nat. Commun.* **6**, 8144 (2015).
 - [20] G. Rogl, P. Sauerstich, Z. Rykavets, V. Romaka, P. Heinrich, B. Hinterleitner, A. Grytsiv, E. Bauer, and

- P. Rogl, *Acta Mater.* **131**, 336 (2017).
- [21] H. Zhu, R. He, J. Mao, Q. Zhu, C. Li, J. Sun, W. Ren, Y. Wang, Z. Liu, Z. Tang, et al., *Nat. Commun.* **9**, 2497 (2018).
 - [22] H. Zhu, J. Mao, Y. Li, J. Sun, Y. Wang, Q. Zhu, G. Li, Q. Song, J. Zhou, Y. Fu, et al., *Nat. Commun.* **10**, 270 (2019).
 - [23] L. Chen, X. Zeng, T. M. Tritt, and S. J. Poon, *J. Electron. Mater.* **45**, 5554 (2016).
 - [24] Y. Tian, H. Zhu, W. Ren, N. Ghassemi, E. Conant, Z. Wang, Z. Ren, and J. H. Ross, Jr., *Phys. Chem. Chem. Phys.* **20**, 21960 (2018).
 - [25] P. Blaha, K. Schwarz, G. K. H. Madsen, D. Kvasnicka, and J. Luitz, *An Augmented Plane Wave+Local Orbitals Program for Calculating Crystal Properties* (Karlheinz Schwarz, Technische Universität Wien, Austria, 2001).
 - [26] E. Papulovskiy, A. A. Shubin, V. V. Terskikh, C. J. Pickard, and O. B. Lapina, *Phys. Chem. Chem. Phys.* **15**, 5115 (2013).
 - [27] G. C. Carter, L. H. Bennett, and D. Kahan, *Metallic shifts in NMR: a review of the theory and comprehensive critical data compilation of metallic materials* (Pergamon, New York, 1977).
 - [28] K. Beshah, D. Zamir, P. Becla, P. A. Wolff, and R. G. Griffin, *Phys. Rev. B* **36**, 6420 (1987).
 - [29] Unpublished work.
 - [30] D. Hobbis, R. P. Hermann, H. Wang, D. S. Parker, T. Pandey, J. Martin, K. Page, and G. S. Nolas, *Inorg. Chem.* **58**, 1826 (2019).
 - [31] Y.-L. Chen and D.-P. Yang, *Mössbauer effect in lattice dynamics: experimental techniques and applications* (Wiley-VCH Verlag, Weinheim, 2007).
 - [32] A. Tavassoli, F. Failamani, A. Grytsiv, G. Rogl, P. Heinrich, H. Müller, E. Bauer, M. Zehetbauer, and P. Rogl, *Acta Mater.* **135**, 263 (2017).
 - [33] N. W. Ashcroft and N. D. Mermin, *Solid state physics* (Holt, Rinehart, and Winston, New York, 1976).
 - [34] J. Toboła, L. Jodin, P. Pecher, H. Scherrer, G. Venturini, B. Malaman, and S. Kaprzyk, *Phys. Rev. B* **64**, 155103 (2001).
 - [35] A. Tavassoli, A. Grytsiv, G. Rogl, V. V. Romaka, H. Michor, M. Reissner, E. Bauer, M. Zehetbauer, and P. Rogl, *Dalton Trans.* **47**, 879 (2018).
 - [36] L. Jodin, J. Tobola, P. Pecher, H. Scherrer, and S. Kaprzyk, *Phys. Rev. B* **70**, 184207 (2004).
 - [37] Y. Obata, *J. Phys. Soc. Jpn.* **18**, 1020 (1963).
 - [38] A. Knigavko, B. Mitrović, and K. V. Samokhin, *Phys. Rev. B* **75**, 134506 (2007).
 - [39] A. K. Koh and D. J. Miller, *At. Data Nucl. Data Tables* **33**, 235 (1985).
 - [40] Y. Yafet and V. Jaccarino, *Phys. Rev.* **133**, A1630 (1964).
 - [41] J. P. Heremans, B. Wiendlocha, and A. M. Chamoire, *Energy Environ. Sci.* **5**, 5510 (2012).
 - [42] H. Kontani and K. Yamada, *J. Phys. Soc. Jpn.* **65**, 172 (1996).
 - [43] H. Kontani and K. Yamada, *J. Phys. Soc. Jpn.* **66**, 2232 (1997).